Computers and Geotechnics 192 (2026) 107882

Contents lists available at ScienceDirect

Computers and Geotechnics

journal homepage: www.elsevier.com/locate/compgeo

Research Paper

Mitigation of Liquefaction Risk in Layered Soils via Stone Column Drains: Numerical Study and Novel Uncoupled Approach

Gabriele Boccieri [a,*], Domenico Gaudio [b], Pedro Arduino [c], Riccardo Conti [a]

[a] Dept. of Civil Engineering and Computer Science Engineering, Università degli Studi di Roma Tor Vergata, Via del Politecnico, 1, 00133 Rome, Italy
[b] Dept. of Structural and Geotechnical Engineering, Sapienza Università di Roma, via Eudossiana 18, 00184 Rome, Italy
[c] Dept. of Civil Engineering and Environmental Engineering, University of Washington, Seattle, WA 98195, United States

ARTICLE INFO

Keywords:
Excess pore water pressures
Liquefaction
Drain
Uncoupled approach
Finite Difference implementation
Finite Element analysis
OpenSees

ABSTRACT

This paper investigates the effectiveness of vertical gravel drains for liquefaction mitigation in stratified soil deposits, emphasising the overlooked hydro-mechanical interaction with adjacent non–liquefiable layers. A comprehensive series of fully coupled 3D finite element analyses was first conducted in the *OpenSees* framework, modelling a unit cell within an indefinite drain system. Different spacing ratios, soil types, and seismic inputs were examined to provide generality and robustness to the study. The main outcome from the numerical analyses is that gravel drains significantly reduce both the peak excess pore water pressure and the duration of high pore pressures, with the hydraulic conditions imposed by the overlying non-liquefiable layers proving critical, particularly near layer interfaces. To quantify mitigation effectiveness, a new integral, dimensionless parameter was proposed, which conveys both the magnitude and dissipation time of the excess pore water pressures.

As a further outcome, this study extends to axisymmetric conditions a 1D uncoupled approach recently proposed for assessing free–field liquefaction, incorporating improvements to capture non–uniform cyclic loading and frequency variations induced by pore pressure build–up. The methodology couples a nonlinear total stress seismic response analysis with an iterative excess pore pressure computation using the Stockwell transform, implemented via a Finite Difference scheme in *Matlab*. Successful validation against the benchmark fully coupled 3D analyses proves that the uncoupled approach can be effectively adopted with low computational cost.

1. INTRODUCTION

Seismic-induced excess pore water pressures in saturated sandy soils can cause severe damage to buildings and civil infrastructure, as observed during the 2010–11 Christchurch (New Zealand, Cubrinovski et al., 2019) and the 2023 Kahramanmaraş (Turkey, Bol et al., 2024; Flora et al., 2024; Moug et al., 2024) earthquakes. Liquefaction risk can be mitigated by different techniques, such as jet grouting (Martin et al., 2004; Croce et al., 2014), artificially induced partial saturation (Mele et al., 2019), vertical prefabricated (Howell et al., 2012), and stone column (Adalier & Elgamal, 2004) drains. Among these, gravel drains are often preferred, due to their relatively low environmental impact (García-Torres & Madabhushi, 2019), moderate cost, as well as simple construction procedures.

Several numerical and experimental studies have demonstrated the effectiveness of gravel drains in mitigating liquefaction (Brennan & Madabhushi, 2002; Elgamal et al., 2009; Bouckovalas et al., 2011; García-Torres & Madabhushi, 2019; Minaka et al., 2021; Bessette et al., 2025). Nonetheless, their design still relies upon simplified procedures, mostly based on the uncoupled, stress-based approach proposed by Seed & Booker (1977). The latter introduces several simplifying assumptions to compute seismic-induced excess pore water pressures, namely: (*i*) purely horizontal axisymmetric water flow towards the drain; (*ii*) infinitely permeable drain; and (*iii*) adopting empirical relations based on undrained cyclic laboratory tests (Seed et al., 1975).

Although the simplified approach by Seed & Booker (1977) has been improved over the years to account for both vertical and horizontal water flow and the finite permeability of gravel drains (Onoue, 1988), as well as by modifying the governing equation (Bouckovalas et al., 2011), some key features are still not considered, such as: the representation of the irregular shear stress time histories, $\tau(t)$, through an equivalent number of uniform stress cycles; the modification of the frequency content of ground motion when liquefaction is triggered; and the influence of soil layering. As for the latter, the role of the hydraulic

* Corresponding author.
E-mail address: gabriele.boccieri@uniroma2.it (G. Boccieri).

https://doi.org/10.1016/j.compgeo.2025.107882
Received 15 October 2025; Received in revised form 27 November 2025; Accepted 28 December 2025
Available online 3 January 2026

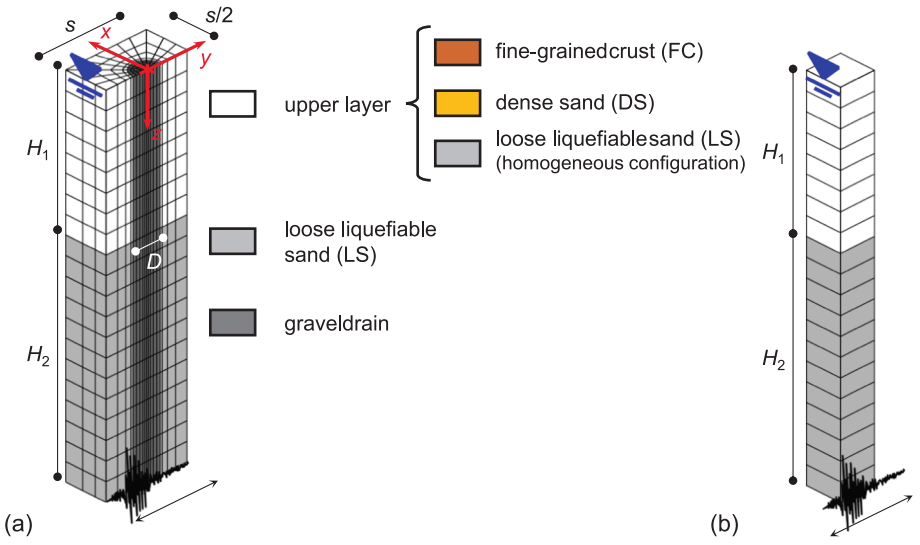

Fig. 1. 3D numerical models implemented in the *OpenSees* framework: half unit cell (a) and free-field soil column (b).

interaction between liquefiable and non-liquefiable layers in the liquefaction assessment of free-field soil deposits has been extensively highlighted in the recent literature (Sinatra & Foti, 2015; Cubrinovski et al., 2019; Cubrinovski & Ntritsos, 2023; Adamidis & Anastasopoulos, 2024). In particular, based on observations from liquefaction case histories after the 2010–11 Christchurch earthquakes and results from nonlinear dynamic analyses, Cubrinovski & Ntritsos (2023) emphasised the significant influence of adjacent layers on the generation and dissipation of earthquake-induced excess pore water pressures, introducing the concept of "system behaviour". This key aspect was explored only recently by Bessette et al. (2025) with reference to gravel drains, by employing 3D fully coupled Finite Element (FE) analyses validated against centrifuge tests. The Authors highlighted the importance of considering realistic soil profiles and interlayer interactions (*system behaviour*), showing that the drainage effectiveness of stone column drains strongly depends on soil stratigraphy.

In light of the considerations above, this study has two main objectives: (*i*) improving the understanding of the physical aspects affecting the effectiveness of vertical gravel drains in layered soil deposits and (*ii*) proposing a novel uncoupled method for their design. To this end, a 3D fully coupled FE parametric study was first performed in *OpenSees* (McKenna et al., 2000), considering an indefinite system of drains embedded in a two-layers soil deposit. Numerical results were then used to validate the Finite Difference (FD) implementation in a *Matlab* (Mathworks Inc., 2021) routine of a novel stress–based uncoupled approach for computing excess pore water pressures in an axisymmetric configuration with vertical gravel drains. Building on the assumptions firstly introduced by Onoue (1988), the proposed method extends the 1D uncoupled approach recently introduced by Boccieri et al. (2024) in order to assess the liquefaction risk in the presence of a drain installed in a layered soil column, accounting for a non–uniform distribution of equivalent loading cycles throughout the earthquake duration, and the modification of the frequency content of ground motion.

2. 3D fully coupled FE analyses

Fig. 1a shows the 3D numerical domain, where a single, half unit cell was modelled to represent an indefinite system of gravel drains, taking advantage of the problem symmetry (Elgamal et al., 2009; Asgari et al., 2013; Tang et al., 2016). The soil column is composed of a deep liquefiable sand underlying a shallow layer. The thickness of the two layers was kept constant, with $H_2 = 6$ m for the liquefiable sand and $H_1 = 4$ m for the upper layer, resulting in a total height of the soil column $H = H_1 + H_2 = 10$ m. The water table is located at the ground surface, and the initial pore water pressure regime is hydrostatic. The diameter of the drain was fixed ($D = 0.80$ m), while different spacing ratios were considered ($s/D = 2$, 3, and 4), where s is the distance between the axes of two adjacent drains.

Three soil types were considered for the upper layer, that is: a fine-grained crust (FC); a dense sand (DS); and a loose liquefiable sand (LS), the latter corresponding to the case of a homogeneous soil deposit. Tab. 1 summarises the physical and mechanical properties assumed for the soil layers and the gravel drain.

Fig. 2 shows the eight acceleration time histories applied at the bottom of the 3D model in the numerical analyses, together with the corresponding Fourier Amplitude spectra. The seismic inputs are characterised by different amplitude, frequency content and significant duration. Tab. 2 lists the relevant ground motion parameters.

The 3D numerical domain was discretised with 1800 *SSPBrickUP* eight–node hexahedral elements (McGann et al., 2015), with a physically stabilised single–point integration and based on the *u–p* formulation (Zienkiewicz et al., 1980). The height of all elements is $h = 0.50$ m, which was selected to avoid numerical distortion of the propagating waves and to ensure their accurate representation within the model

Tab. 1
Physical and mechanical properties of soils.

soil	γ_{sat}	PI	e_{min}	e_{max}	e	D_R	ϕ'_{cv}	s_u	ν	$k_{v,h}$
	kN/m^3	%	–	–	–	%	°	kPa	–	m/s
gravel (drain)	21.10	–	0.435	0.923	0.550	76	37.0	–	0.33	$1\bullet10^{-2}$
fine-grained crust (FC)	17.70	30	–	–	–	–	0.0	40	0.48	$1\bullet10^{-7}$
dense sand (DS)	19.20	–	0.660	1.000	0.720	82	31.5	–	0.33	$1\bullet10^{-4}$
liq. sand (LS)	18.50	–	0.660	1.000	0.854	43	31.5	–	0.33	$1\bullet10^{-4}$

γ_{sat} = saturated unit weight; PI = plasticity index; e_{min} = minimum void ratio; e_{max} = maximum void ratio; e = initial void ratio; $D_R = (e_{max} - e)/(e_{max} - e_{min})$ = relative density; ϕ'_{cv} = friction angle at constant volume; s_u = undrained shear strength; ν = Poisson's ratio; $k_{v,h}$ = vertical and horizontal hydraulic conductivity.

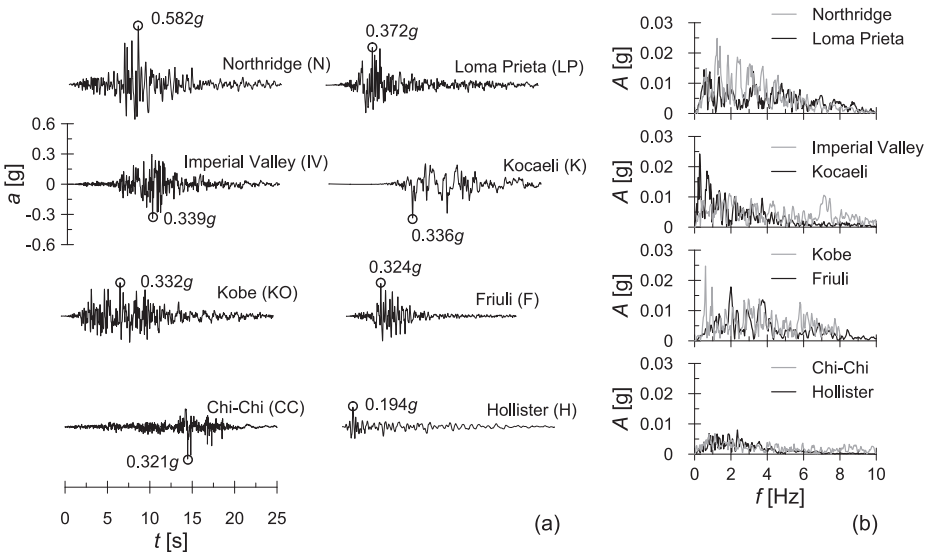

Fig. 2. Acceleration time histories (a) and Fourier amplitude spectra (b) of the seismic recordings considered in the 3D numerical analyses.

Tab. 2
Ground motion parameters of the input acceleration time histories.

earthquake	a_{max}	f_p	f_{mean}	$D_{5–95}$	I_A	T_{rec}
	g	Hz	Hz	s	m/s	s
1994 Northridge (N)	0.582	1.24	2.64	9.0	2.70	25
1989 Loma Prieta (LP)	0.372	0.52	3.26	10.3	1.26	25
1979 Imperial Valley (IV)	0.339	1.36	4.04	8.58	1.24	25
1999 Kocaeli (K)	0.336	0.28	1.43	10.6	1.24	25
1995 Kobe (KO)	0.332	0.60	3.55	10.95	1.66	25
1976 Friuli (F)	0.324	2.00	3.21	4.20	0.76	20
1999 Chi–Chi (CC)	0.321	1.12	6.41	11.25	0.37	25
1961 Hollister (H)	0.194	2.36	2.13	14.6	0.25	25

a_{max} = peak acceleration; f_p = dominant frequency; f_{mean} = mean square frequency (Rathje et al., 1998); $D_{5–95}$ = strong motion duration (Trifunac & Brady, 1975); I_A = Arias Intensity; T_{rec} = total record duration.

Tab. 3
Summary of the 3D unit cell FE analyses carried out in *OpenSees*.

FE analysis #	Top layer	*s/D*	seismic input	*SF*	a_{max}•*SF*
	–	–	–	–	g
1–9	FC, DS, LS	2, 3, 4	N	1	0.582
10–18	FC, DS, LS	2, 3, 4	CC	1.58	0.506
19–27	FC, DS, LS	2, 3, 4	LP	1	0.372
28–36	FC, DS, LS	2, 3, 4	IV	1	0.339
37–45	FC, DS, LS	2, 3, 4	K	1	0.336
46–54	FC, DS, LS	2, 3, 4	KO	1	0.332
55–63	FC, DS, LS	2, 3, 4	F	1	0.324
64–72	FC, DS, LS	2, 3, 4	CC	1	0.321
73–81	FC, DS, LS	2, 3, 4	LP	0.602	0.224
82–90	FC, DS, LS	2, 3, 4	H	1	0.194
91–99	FC, DS, LS	2, 3, 4	KO	0.280	0.093

(Kuhlemeyer & Lysmer, 1973). The aspect ratio of the largest element is 1.35, well within the typical recommended limit of 5 (Potts & Zdravković, 1999). Given the mechanical properties adopted for soils and drain, the geometry of the problem, and the frequency content of the applied earthquakes, the *u–p* formulation provides a reliable representation of the coupled hydro–mechanical dynamic problem (Zienkiewicz et al., 1980).

The analyses were performed in two stages: a geostatic phase, in which the gravel drain was wished in place and the gravitational acceleration was imposed to define the initial stress state, followed by a dynamic calculation phase, where the horizontal acceleration time histories were applied to the bottom nodes of the domain ($z = H$ in Fig. 1a), along the *y*–direction. Displacements were restrained for all nodes belonging to the *y–z* plane boundaries along the out-of-plane direction ($d_x = 0$ at $x = 0$ and $s/2$), while periodic constraints were applied to the nodes on the *x–z* planes along the direction of the input motion ($\Delta d_y = 0$ at $y = \pm s/2$). All nodes at the bottom of the model were fully fixed ($d_x = d_y = d_z = 0$ at $z = H$) during the static calculation phase. As for the hydraulic boundary conditions, the vertical and the bottom boundaries were set as impervious, while null pore water pressures were set at the water table level.

To assess the efficiency of gravel drains, a further set of FE analyses was carried out on a 10-m-high free-field soil column (without drains, Fig. 1b), which represents the pertinent two-layered deposit subjected to the same seismic inputs. The soil column was discretised using 20 *SSPBrickUP* eight–node hexahedral elements, with the same hydraulic and mechanical boundary conditions as those imposed for the 3D unit cell.

All 3D FE analyses performed in this study are listed in Tab. 3, for a total of 99 analyses with the 3D unit cell and additional 33 free-field soil column analyses. As reported in Tab. 3, some of the input motions, characterised by similar values of the strong motion duration, $D_{5–95}$, but different intensities, were scaled, using suitable scaling factors (*SF*) to investigate the combined influence of earthquake intensity and duration on the resulting excess pore water pressures.

The *SANISAND* constitutive model (Dafalias & Manzari, 2004) was adopted to describe the mechanical behaviour of the liquefiable and the dense sand, while the *Pressure Independent Multi–Yield* (*PIMY*, Yang et al., 2008; Gu et al., 2011) and the *Pressure Dependent Multi–Yield 02* (*PDMY02*, Yang et al., 2003) models were employed to reproduce the cyclic response of the FC layer and the gravel drain, respectively.

The *SANISAND* constitutive model was calibrated to reproduce the dynamic behaviour of the Hostun HN31 sand. Starting from the work by Gaudio et al. (2023), model parameters were calibrated based on the results of monotonic and cyclic laboratory tests presented by Azeiteiro et al. (2017) and De Gennaro et al. (2004).

The *PDMY02* parameters defining the relationship between the small–strain shear modulus and the mean effective stress, $G_0(p')$, were calibrated based on the empirical equation proposed by Nishio et al. (1985) for gravels. The remaining parameters were calibrated based on the damping and decay curves proposed by Seed & Idriss (1970). Finally, the constitutive parameters governing the dilatant and contractive behaviour of the soil were set to prevent the generation of excess pore

Tab. 4
Parameters adopted in the *SANISAND* constitutive model for the sandy layers.

G_0	ν	M	c	λ_c	e_0	ξ	m	h_0	c_h	n^b	A_0	n^d	z_{max}	c_z
-	-	-	-	-	-	-	-	-	-	-	-	-	-	-
293	0.05	1.265	0.711	0.07	1.00	0.36	0.02	2.90	0.968	1.64	0.15	3.50	10	1000

Tab. 5
Parameters adopted in the *PDMY02* constitutive model for the gravel drain.

G_r kPa	K_r kPa	p'_r kPa	n –	γ_{max} –	ϕ °	λ_c –	e_0 –	ξ –	ϕ_{PT} °
$12.08 \bullet 10^4$	$31.49 \bullet 10^4$	101	0.44	0.1	37	0.02	0.90	0.70	26
c_1	c_2	c_3	d_1	d_2	d_3	liq_1	liq_2	NYS	
–	–	–	–	–	–	–	–	–	
0.013	5.0	0.0	0.3	3.0	0.0	1.0	0.0	20	

Tab. 6
Parameters adopted in the *PIMY* constitutive model for the FC layer.

G_r kPa	K_r kPa	p'_r kPa	n –	γ_{max} –	ϕ °	c kPa	NYS –
$2.98 \bullet 10^4$	$7.35 \bullet 10^5$	100	0.0	0.1	0.0	40	20

water pressures within the gravel drain (Yang et al., 2008).

The *PIMY* model parameters were calibrated against the decay and damping curves proposed by Vucetic & Dobry (1991), considering a Plasticity Index, $PI = 30$ %, and an overconsolidation ratio, $OCR = 3$. The small–strain shear modulus was set constant within the FC layer, while the bulk modulus is consistent with a Poisson's ratio $\nu = 0.48$, approximating the undrained response of the clayey crust. Tabs. 4, 5, and 6 present the values of the constitutive parameters considered for the *SANISAND*, *PMY02* and *PIMY* models, respectively.

2.1. Effectiveness of gravel drains – 3D FE results

Fig. 3 shows the FE results for three layouts, characterised by the presence of a shallow layer of fine–grained soil, dense sand and loose sand, respectively, all excited by the 1999 Chi–Chi (CC) earthquake ground motion. Specifically, the results of the 3D unit cells analyses ($s/D = 3$) are compared with those from the corresponding 1D free-field analyses, in terms of space–time contours of the excess pore water pressure ratio, $r_u(z,t) = u(z,t)/\sigma'_{v0}(z)$, where $u(z,t)$ is the excess pore water pressure and $\sigma'_{v0}(z)$ is the geostatic vertical effective stress. For the 3D analyses, results are reported along the vertical axis at $x = s/2$ and $y = 0$ (red lines in Fig. 3). In the 1D free-field soil column with the fine-grained crust (Fig. 3a), full liquefaction is reached in most of the liquefiable sand soon after the onset of shaking. Moreover, a negligible redistribution of excess pore water pressures occurs in the upper soil after the strong motion stage, due to its low hydraulic conductivity. Conversely, when the free-field column includes a shallow dense or loose sand layer, a non–negligible amount of excess pore water pressures

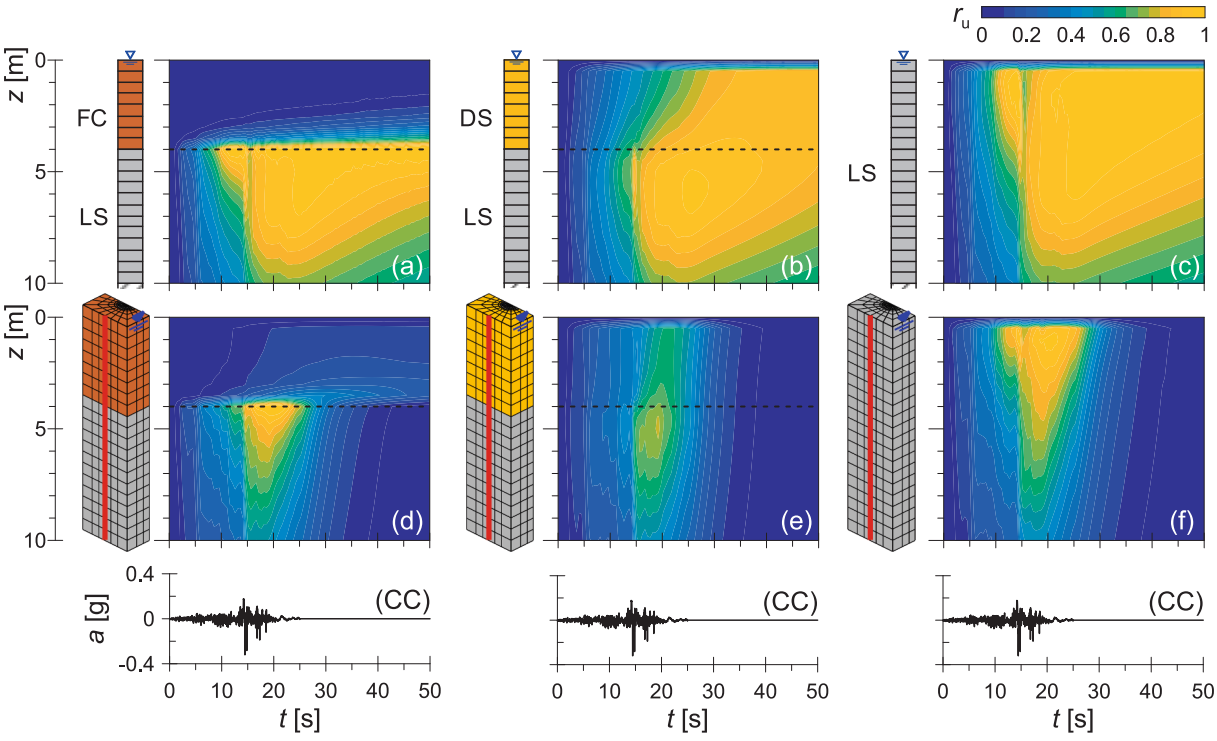

Fig. 3. Space–time contours of the excess pore water pressure ratio (CC motion) from the 1D free-field soil column (a, b, c) and the 3D unit cell analyses ($s/D = 3$, d, e, f), for different shallow layers: fine-grained (a, d); dense (b, e) and loose sand (c, f).

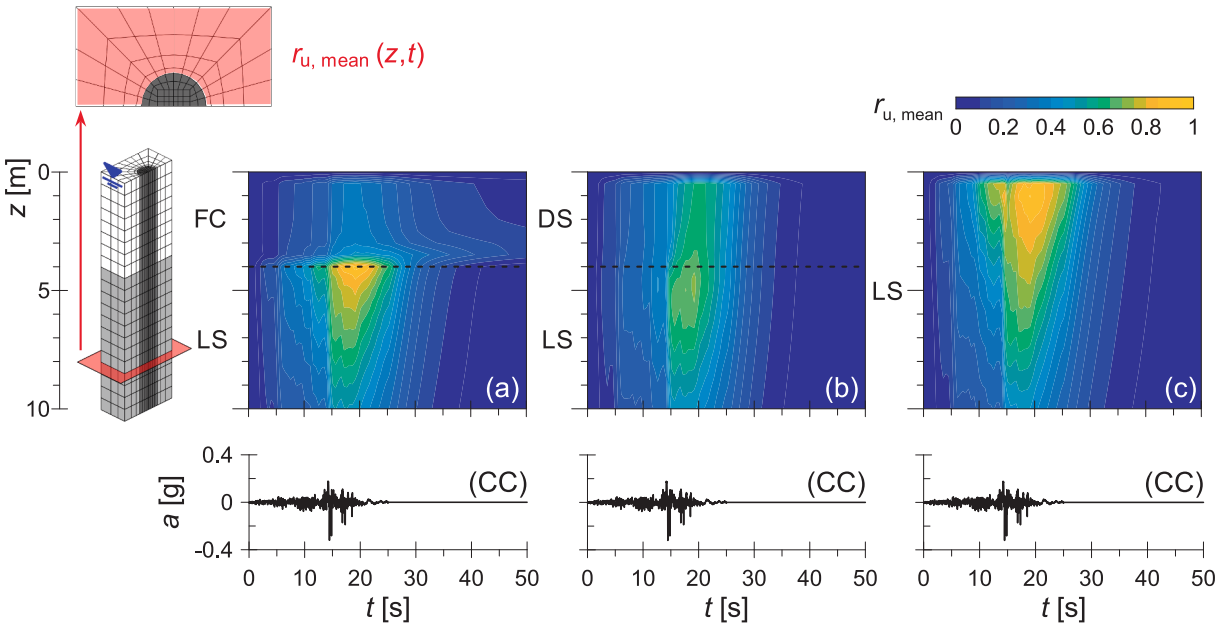

Fig. 4. Space–time contours of the mean excess pore water pressure ratio, $r_{u,\,mean}(z,t)$, from the 3D unit cell analyses (CC motion and $s/D = 3$), for different shallow layers: fine-grained (a); dense (b) and loose sand (c).

is also generated close to the soil surface, until complete liquefaction is triggered. In the case of the dense sand (Fig. 3b), liquefaction in the upper portion of the column is delayed compared to that in the deeper loose sand, being significantly influenced by the upward redistribution of excess pore water pressures. By contrast, in the homogeneous profile (Fig. 3c) the generation of excess pore water pressures is nearly uniform throughout the soil column. The presence of the gravel drain (Figs. 3d, e, and f) reduces the differences between the various scenarios remarkably. In all three layouts, a rapid dissipation phase begins before the end of shaking, preventing liquefaction to happen in most of the deep layer.

In the presence of a fine-grained crust, the horizontal water flow driven by the gravel drain across the whole sand layer effectively limits the extent of full liquefaction within the deepest part of the loose sand. However, excess pore water pressures accumulation just below the FC layer indicates the presence of a non–negligible vertical flow, in contrast with the common assumption of a purely horizontal flow towards the drain (Seed & Booker, 1977). In the case of a dense sand layer (Fig. 3e), liquefaction is prevented throughout the soil domain, while, in the case

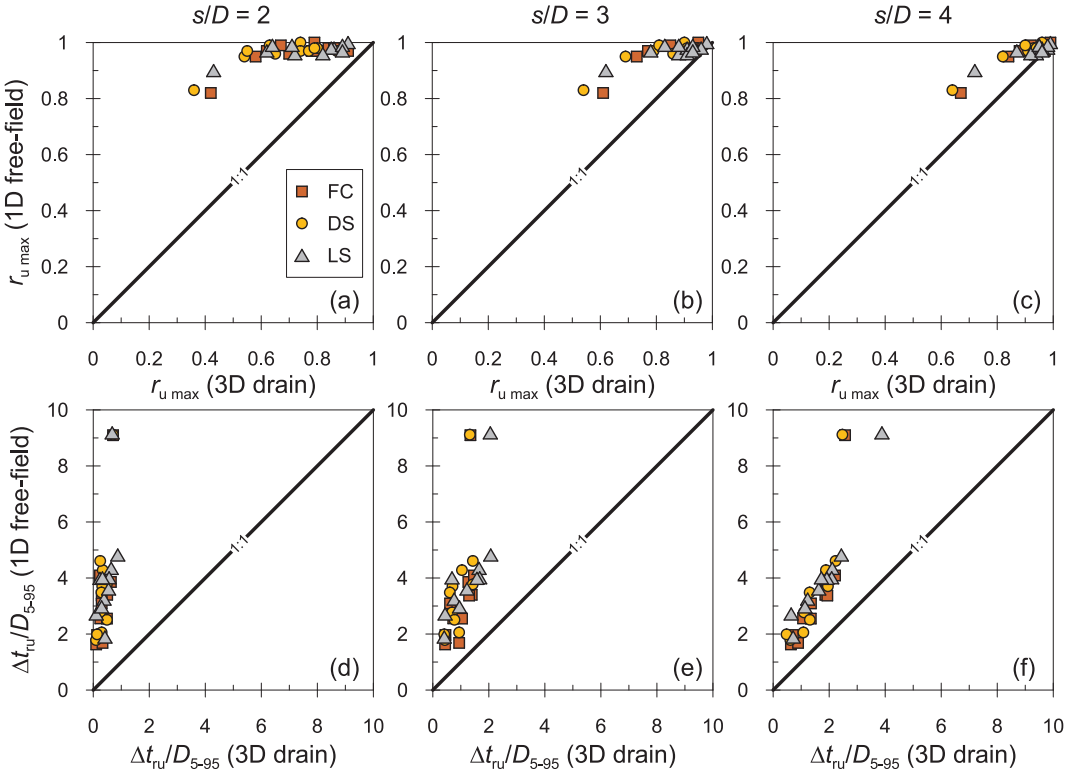

Fig. 5. Comparison between the results obtained at the mid-depth within the liquefiable soil layer for the 3D unit cell and the 1D free-field soil column.

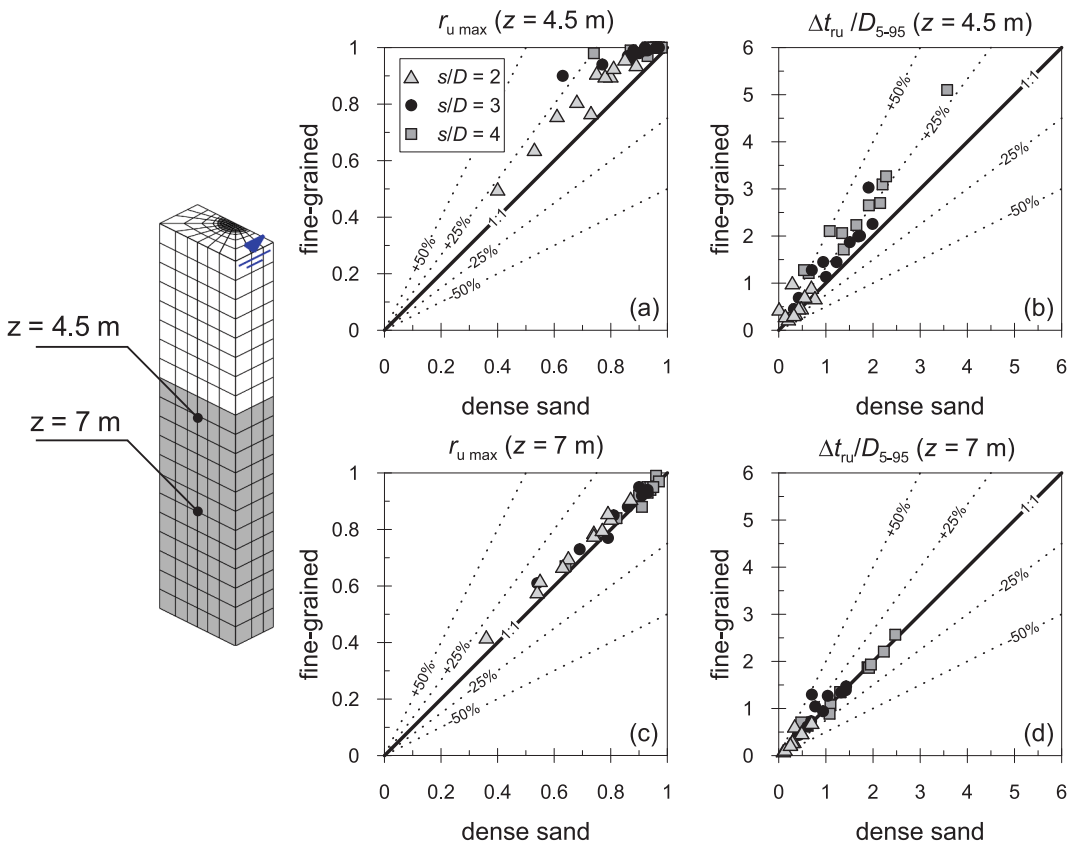

Fig. 6. Main results obtained near the crust (a, b) and at the centre of the liquefiable soil (c, d), considering a fine–grained or a dense sand as the shallow layer.

of a homogeneous loose sand deposit (Fig. 3d), full liquefaction is triggered close to the soil surface for a short period of time, which may be ascribed to the combination of the vertical flow and the low confining stresses at these depths.

Fig. 4 refers to the same 3D configurations discussed in Figs. 3d, e and f, showing the mean excess pore water pressure ratio, $r_{u,\,mean}(z,t)$, computed at each depth within the soil, instead of referring to a specific vertical axis. As illustrated in the figure, $r_{u,\,mean}(z,t)$ corresponds to the average value of $r_u(z,t)$ over the red–shaded surface of the soil domain. The space–time contours show slight differences compared to Fig. 3, with marginally lower values of excess pore pressures over time.

The results shown in Figs. 3 and 4 highlight the two main advantages provided by gravel drains, such as the reduction of (*i*) the magnitude of excess pore water pressures, and (*ii*) the time needed for their dissipation. Simple and physically sound parameters can be introduced to convey information about the severity of the liquefaction phenomenon and the efficiency of the drainage system, namely the maximum excess pore water pressure ratio, $r_{u\,max}$, and the time interval, Δt_{ru}, over which the excess pore water pressure ratio is close to $r_{u\,max}$, both computed at key depths within the soil deposit. Specifically, Δt_{ru} has been defined as the interval between the first and the last time instants at which $r_u = 0.90 \cdot r_{u\,max}$.

In Fig. 5, a comparison between the 1D free–field and the 3D unit cell analyses is made in terms of $r_{u\,max}$ and Δt_{ru}, the latter normalised by the strong motion duration of the seismic input, $D_{5\text{-}95}$. Both parameters are computed at the mid-depth of the liquefiable soil layer ($z = H_1 + 0.5 \bullet H_2 = 7$ m for the layered soil deposit and $z = 5$ m for the case of the homogeneous liquefiable layer) and at $x = s/2$, $y = 0$, in the 3D unit cells. Each pair of charts refers to a specific geometrical configuration of the 3D unit cell ($s/D = 2$ in Fig. 5 a and d; $s/D = 3$, b and e; $s/D = 4$, c and f), and pertains to different soil layouts. As expected, the results show a reduction in the drainage efficacy for an increasing spacing ratio s/D, both in terms of r_{umax} and $\Delta t_{ru}/D_{5\text{-}95}$. In most of the configurations with $s/D = 2$, the drain prevents the attainment of complete liquefaction and $\Delta t_{ru}/D_{5\text{-}95}$ is always less than 1, which means that high excess pore water pressures are dissipated right before the end of the strong-motion duration. In the layouts with $s/D = 3$ and $s/D = 4$, $r_{u\,max}$ is similar to that from the 1D free-field analyses, indicating complete liquefaction in some cases (particularly when $s/D = 4$). However, $\Delta t_{ru}/D_{5\text{-}95}$ is smaller than in the free-field case, confirming that the gravel drain still enhances the dissipation process.

Fig. 6 presents a comparison of $r_{u\,max}$ and $\Delta t_{ru}/D_{5\text{-}95}$ obtained at two different depths within the soil deposit, namely close to the boundary with the upper layer ($z = 4.5$ m, $x = s/2$ and $y = 0$; Figs. 6a and b) and at the mid-depth within the liquefiable layer ($z = 7$ m, $x = s/2$ and $y = 0$; Figs. 6c and d). The two configurations with fine-grained crust (FC) and dense sand (DS) shallow layers are analysed, for different spacing ratios. At the centre of the liquefiable layer ($z = 7$ m), a small influence of the upper soil is observed, as the vertical flow is negligible compared to the predominant horizontal flow towards the gravel drain. Conversely, close to the boundary between the two layers ($z = 4.5$ m), higher values of both $r_{u\,max}$ and $\Delta t_{ru}/D_{5\text{-}95}$ are computed in the presence of a fine-grained crust if compared with the DS configurations, with average values increasing by about 12 % and 40 %, respectively. This observation indicates the presence of a vertical flow towards the non-liquefiable layer and demonstrates that assuming a purely horizontal flow is unrealistic. The results therefore confirm that the influence of the non-liquefiable crust cannot be neglected when assessing drain efficiency, and that the entire soil domain should be considered for a proper design of gravel drains.

2.2. A novel integral index to assess drain efficiency

To capture the overall response of the soil deposit in free-field conditions, Ntritsos & Cubrinovski (2024) introduced a dimensional Pore Pressure Index (*PPI*), defined as:

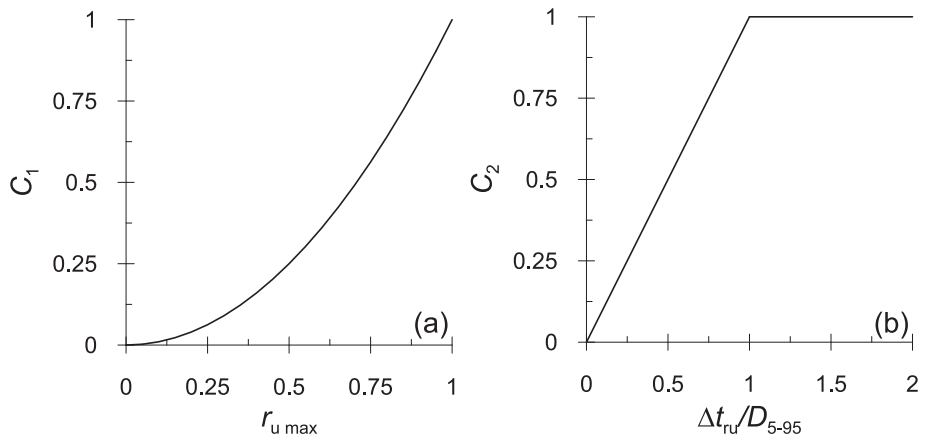

Fig. 7. Functions for evaluating the integral index *LAI* (Eqs. (3) and (4)).

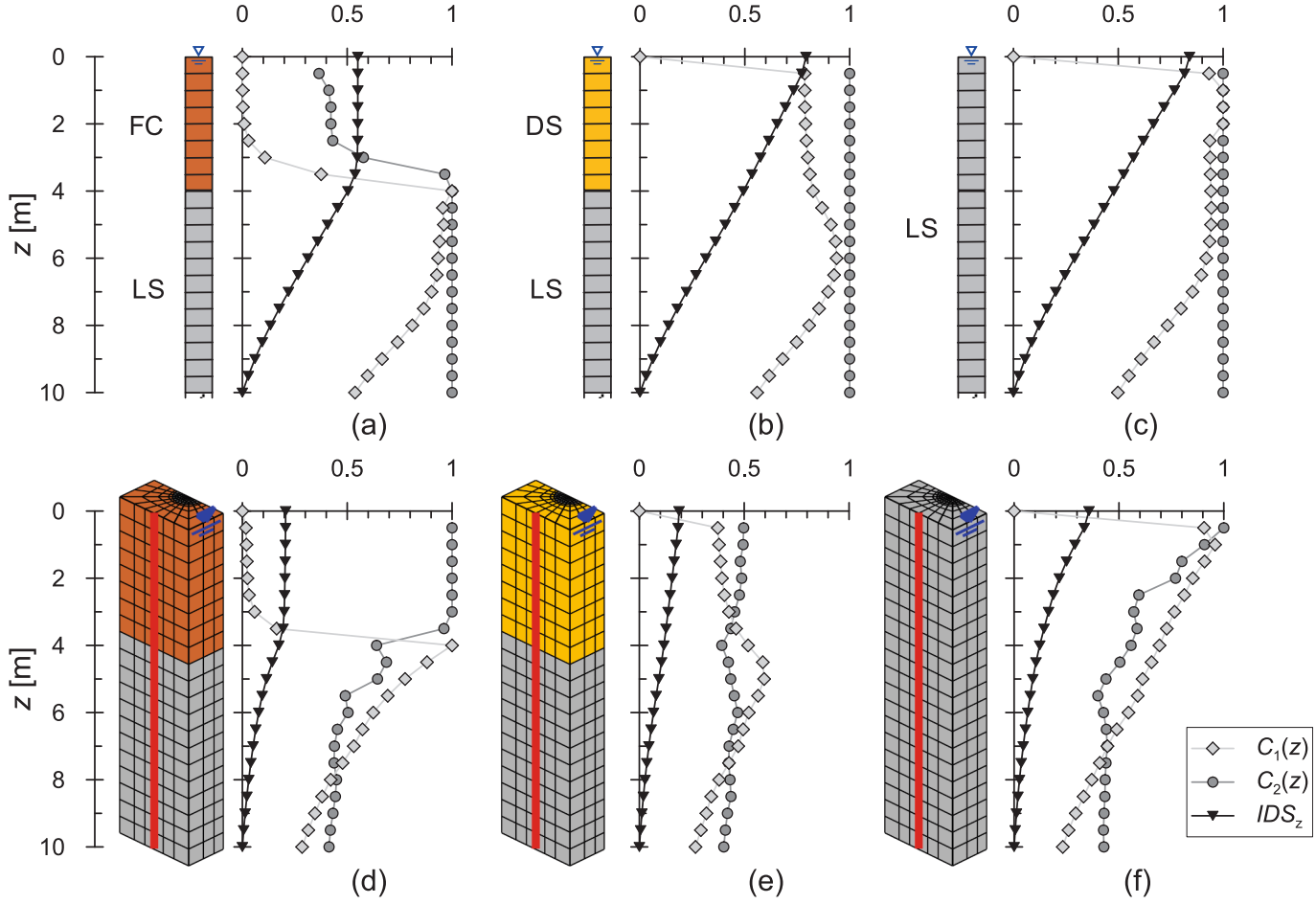

Fig. 8. Functions to determine the severity of the seismic-induced excess pore water pressures in the free-field soil column (a, b, c) and 3D unit cell for the analyses # 67, 68 and 69 (d, e, f).

$$PPI = \sum_{i=1}^{n} W_i \bullet t_i \bullet r_{u\ max,i} \tag{1}$$

where n is the total number of layers within the top 10 m of soil; W_i is a binary weighting factor ($W_i = 0$ if the i^{th} layer is either non–liquefiable or located above the water table; $W_i = 1$ otherwise); and t_i is the thickness of the i^{th} layer. While *PPI* provides a clear picture of the severity of liquefaction and quantifies the total amount of excess pore water pressures generated throughout the soil column, it does not account for any possible redistributions within the non–liquefiable layers, due to the sharp assumption $W = 0$. Moreover, *PPI* does not contain any information about the system dissipation capacity in the presence of gravel drains.

To address the above limitations and to include an indication of the system efficiency in the presence of drains, a new dimensionless integral Liquefaction Assessment Index, *LAI*, is here defined as:

$$LAI = -\frac{1}{H} \bullet \int_{H}^{0} C_1(z) \bullet C_2(z) \bullet dz \tag{2}$$

where C_1 and C_2 are functions of $r_{u\,max}$ and Δt_{ru}, respectively, as follows:

$$C_1(z) = r_{u\,max}(z)^2 \tag{3}$$

$$C_2(z) = \begin{cases} \dfrac{\Delta t_{r_u}(z)}{D_{5-95}} & if\ \Delta t_{r_u}(z) < D_{5-95} \\ 1 & if\ \Delta t_{r_u}(z) \geq D_{5-95} \end{cases} \tag{4}$$

By definition, the integral index *LAI* varies between zero and one. This range is useful for a quick assessment of the severity of liquefaction, where $LAI = 1$ indicates a critical configuration, *e.g.*, a poor drain efficiency. A quadratic function was adopted for C_1 to give less weight to small values of $r_{u\ max}$, as shown in Fig. 7. It is worth noting that a depth–dependent weighting, which would give greater importance to excess pore water pressures generated in shallower layers, was not applied. This choice was adopted to define a simple index that represents the overall response of the soil deposit and the drain system concisely. Nonetheless, this assumption might be reconsidered in a more design–oriented context.

Fig. 8 illustrates the application of the proposed *LAI* to the numerical results discussed in Fig. 3. For further information, function LAI_z is also introduced, as defined by Eq. (2) but calculated up to the generic depth z. Profiles of $C_1(z)$, $C_2(z)$ and LAI_z are reported for both the 1D free-field soil column and the 3D unit cell along the vertical alignment considered previously. In the 1D free-field soil column with a fine–grained crust (Fig. 8a), liquefaction occurs in most of the liquefiable sand and lasts over a time interval that exceeds the strong motion duration ($\Delta t_{ru}/D_{5-95} > 1$), resulting in an integral parameter $LAI = 0.55$. The function LAI_z remains constant through the fine-grained crust, reflecting the negligible excess pore water pressure in the shallow layer, as effectively captured by the $C_1(z)$ function. When a shallow dense sandy layer is present (Fig. 8b), the upward flow increases the severity of the phenomenon, as indicated by the higher value of the integral index ($LAI = 0.79$). This case highlights the importance of considering the full system behaviour rather than limiting the assessment of the integral parameters to the sole liquefiable layers. In the homogeneous liquefiable deposit (Fig. 8c), full liquefaction of almost the entire soil column results in an integral index $LAI = 0.84$, indicating an extremely severe condition.

The presence of vertical gravel drains (Figs. 8d, e, and f) significantly reduces the extent of liquefaction in most of the soil deposit, for all three configurations, and accelerates the dissipation process ($C_2 < 1$). The corresponding *LAI* are equal to 0.21, 0.19, and 0.36, for the cases with the fine–grained crust, the dense sand and a loose sandy layer, respectively.

3. A novel uncoupled approach

With the aim of developing a simplified method to assess the effectiveness of gravel drains in mitigating liquefaction, the uncoupled approach recently proposed by Boccieri et al. (2024) for computing seismic-induced excess pore water pressures within a 1D free-field stratified soil column (Appendix A) was extended to an axisymmetric configuration to represent a 3D indefinite system of drains.

Following Onoue (1988), the governing diffusion equation to solve is:

$$\frac{\partial u(z,r,t)}{\partial t} = c_{vr} \bullet \left(\frac{\partial^2 u(z,r,t)}{\partial r^2} + \frac{1}{r} \bullet \frac{\partial u(z,r,t)}{\partial r} \right) + c_{vz} \bullet \frac{\partial^2 u(z,r,t)}{\partial z^2} + \frac{\partial u_g(z,r,t)}{\partial t} \tag{5}$$

where r is the radial distance from the centre of the drain and z is the depth measured from the ground surface (Fig. 9). The first and the second term on the right–hand side of Eq. (5) are dissipative terms, which are proportional to the radial and vertical consolidation coefficients, c_{vr} and c_{vz}, while the third one is the source term, which represents the rate of excess pore water pressures occurring in fully undrained conditions. The two consolidation coefficients are computed as functions of the current mean effective stress p', as $c_{vr} = k_h/(m_v(p') \bullet \gamma_w)$ and $c_{vz} = k_v/(m_v(p') \bullet \gamma_w)$, where k_h and k_v are the horizontal and vertical hydraulic conductivity of the soil, respectively, and $m_v(p')$ is the pressure–dependent coefficient of volume compressibility.

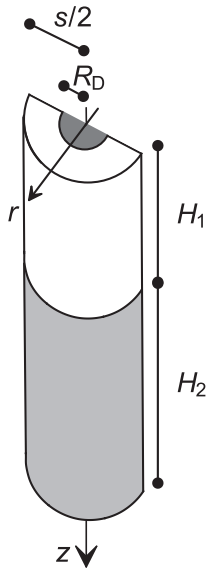

Fig. 9. Problem layout in its axisymmetric configuration.

Onoue (1988) solved Eq. (5) considering: (*i*) null initial excess pore water pressures ($u(z,r,t=0) = 0$); (*ii*) null excess pore water pressures at the ground water table ($u(z = z_w,r,t) = 0$); (*iii*) impervious boundary conditions at the bottom of the domain ($\partial u(z = H,r,t)/\partial z = 0$) and at the maximum distance from the drain ($(\partial u(z,r = s/2,t)/\partial r = 0$); and (*iv*) a flow continuity condition at the drain–soil interface, which corresponds to solve the following equation:

$$\frac{k_{vD}}{k_{hS}} \bullet \frac{R_D}{2} \bullet \left.\frac{\partial^2 u}{\partial z^2}\right|_{r=R_D} + \left.\frac{\partial u}{\partial r}\right|_{r=R_D} = 0 \tag{6}$$

where k_{vD} and k_{hS} are the vertical and horizontal hydraulic conductivities of the drain and the soil, respectively. In the case of a stratified soil deposit, the flow continuity must be imposed at the interface between two adjacent layers, given by:

$$\lim_{z \to H_1^-} k_{v1} \frac{\partial u}{\partial z} = \lim_{z \to H_1^+} k_{v2} \frac{\partial u}{\partial z} \tag{7}$$

where k_{v1} and k_{v2} are the vertical hydraulic conductivities of the upper and lower layers, respectively, and the limit operators indicate the approach to $z = H_1$ from the top (H_1^-) and the bottom (H_1^+).

Building on the assumptions introduced by Onoue (1988), the method developed in this paper was implemented in a *Matlab* (Mathworks Inc., 2021) routine using the Finite Difference Method (FDM) with an explicit Forward–Time, Centred–Space scheme (FTCS, Recktenwald, 2004). The adopted time and spatial discretization were selected to guarantee the stability of the integration algorithm and to minimise numerical errors. Details of the FDM implementation are provided in Appendix B.

The filtering procedure, introduced by Boccieri et al. (2024) to capture the frequency shift caused by liquefaction in the wave propagation problem, was handled by using the Stockwell transform

Tab. 7
Soil parameters adopted in the total-stress seismic site response analysis (Conti et al., 2020) and in the novel uncoupled approach.

soil	a	b	c	d	χ	θ	CSR_t	β	η
	–	–	–	–	–	–	–	–	–
fine-grained crust (FC)	0.10	10.00	0.13	1.23	–	–	–	–	–
dense sand (DS)	0.73	0.70	0.35	1.58	0.92	1.30	0.023	1.918	0.750
liq. sand (LS)	1.53	0.46	0.27	1.69	0.92	1.30	0.023	0.641	0.750

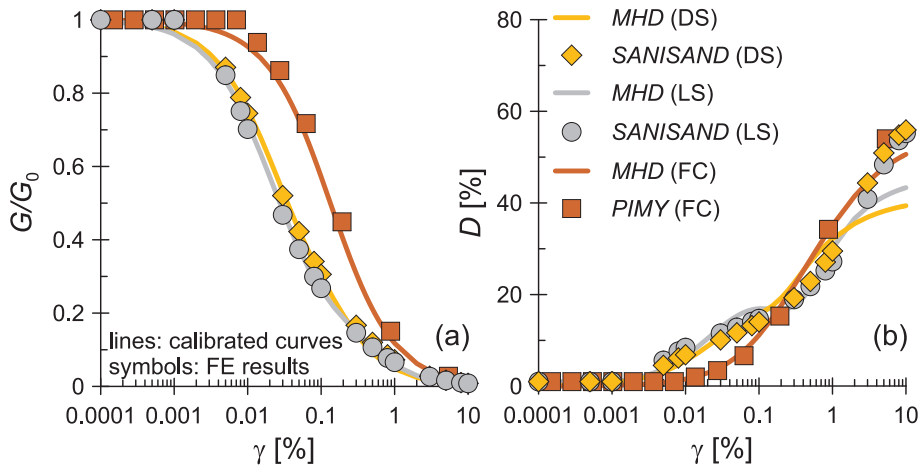

Fig. 10. Shear modulus decay (a) and damping curves (b) adopted in this study (lines) and obtained with simulations of cyclic shear tests in *OpenSees* (symbols).

(Stockwell et al., 1996). The maximum excess pore water pressure ratio, $r_{u\ max}$, computed at the k^{th} iteration at the centre of the deep liquefiable layer (*i.e.*, at $z = H_1 + 0.5 \bullet H_2$ for the layered configuration, and $r = R_D + 0.5 \bullet (s/2 - R_D)$ in Fig. 9), was used to filter the shear stress time histories in the subsequent $(k+1)^{th}$ iteration, $\tau(t)$, at each point within the liquefiable layer. The shear stress time histories, which define the seismic demand for the uncoupled approach, were first derived from a 1D free–field total–stress Seismic Site Response Analysis. As a result, $\tau(t)$ does not vary along the radial direction r.

4. Validation of the uncoupled approach

In this Section, the calibration of the novel uncoupled approach is presented in § 4.1, and a validation against the results of the above 3D fully coupled FE analyses is discussed in § 4.2.

4.1. Calibration of the uncoupled approach

The 1D total-stress site response analysis was performed adopting the *Modified Hardin and Drnevich* (*MHD*) model proposed by Conti et al. (2020), which requires six parameters, namely: the soil shear strength, τ_{lim}, the small strain shear modulus, G_0, two parameters, a and b, controlling the shear modulus decay curve, $G/G_0(\gamma)$, and c and d, which govern the damping curve, $D(\gamma)$. The assumed small–strain shear velocity profiles, $V_{S0}(z)$, were consistent with the small-strain shear stiffness provided by the constitutive model parameters listed in Tabs. 4, 5, and 6.

A series of single-element numerical simulations were carried out in *OpenSees* to calibrate: (*i*) the *MHD* soil model; (*ii*) the cyclic resistance, *CSR*-N_L, and the excess pore water pressure accumulation curves, r_u-r_N, for the loose sand; (*iii*) the *CSR*-N_L curve for the dense sand. The parameters a, b, c, and d were calibrated against the decay and damping curves resulting from strain–controlled drained cyclic shear tests. Tab. 7 lists the computed parameters, while Fig. 10 shows a comparison

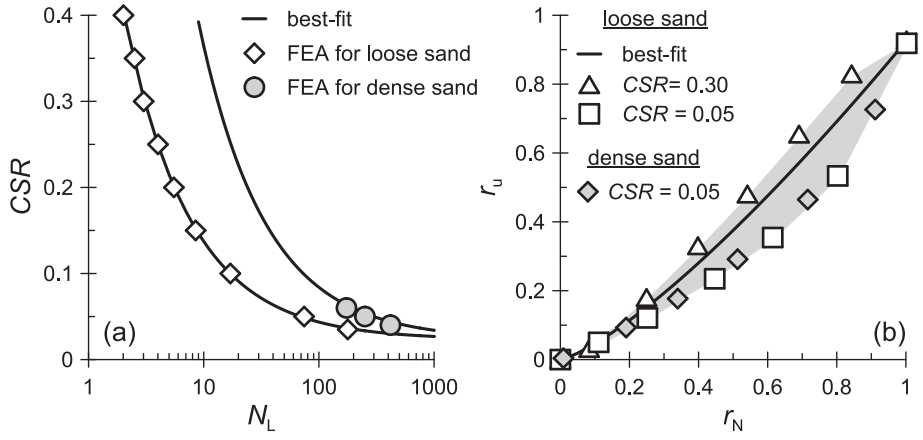

Fig. 11. Cyclic resistance (a, Eq. (8)) and pore water pressure curves (b, Eq. (9)) adopted in the uncoupled approach.

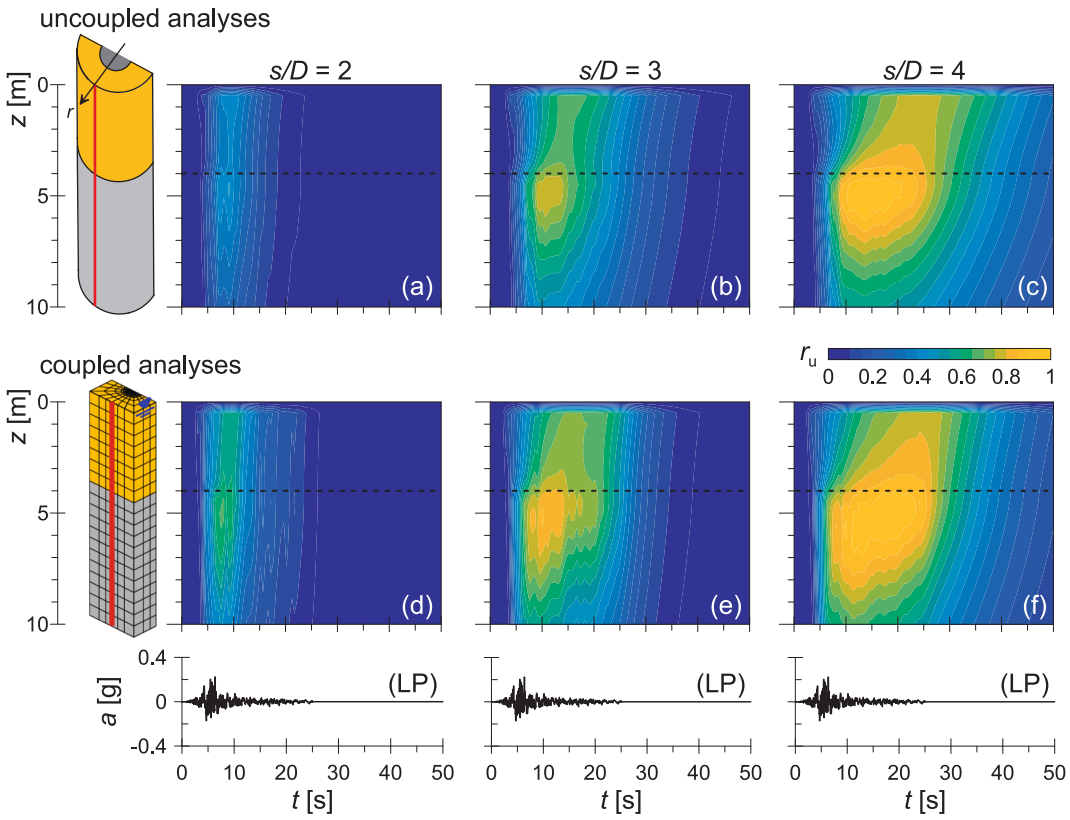

Fig. 12. Space-time contours of the excess pore water pressure ratio in the uncoupled (a, b, c) and coupled analyses (d, e, f), with a dense sand shallow layer and for different values of s/D (seismic input = LP scaled by $SF = 0.602$).

between the reference and the calibrated $G/G_0(\gamma)$ and $D(\gamma)$ curves.

The CSR–N_L and r_u–r_N, curves were described by Eqs. (8) and (9), respectively:

$$CSR = CSR_t + \beta \bullet N_L^{-\eta} \tag{8}$$

$$r_u = \chi \bullet r_N^{\theta} \tag{9}$$

where CSR_t, β, η, x and θ are dimensionless parameters. The curves related to the loose sand were calibrated against the results of stress-controlled undrained cyclic shear tests, with CSR in the range 0.05–0.30 for the r_u–r_N curve and 0.035–0.40 for the CSR–N_L curve, both with $\sigma'_{v0} = 40$ kPa, representative of the initial effective stress state at the mid–depth of a 10-m-high homogeneous loose sand column. The cyclic resistance curve related to the dense sand was calibrated by simulating three stress–controlled undrained cyclic shear tests in *OpenSees* assuming $\sigma'_{v0} = 15$ kPa, this value being representative of the initial effective stress state in the middle of the shallow dense sand, and CSR = 0.04, 0.05, and 0.06. Moreover, the same r_u–r_N curve previously calibrated for the loose sand was adopted for the dense one. Fig. 11 depicts the cyclic resistance and excess pore water pressure accumulation curves considered in the uncoupled analyses, together with the numerical results from the element tests. Similarly, Tab. 7 presents the values of the parameters obtained through the best–fitting of the curves.

4.2. Comparison and outcome of the validation

Fig. 12 presents a comparison of the space–time contours of $r_u(z,t)$, obtained through the FD uncoupled and the FE coupled approach, for different spacing ratios (s/D = 2, 3, and 4), adopting the scaled (SF = 0.602) 1989 Loma Prieta (LP) earthquake as input motion, and considering a dense sand shallow layer (analyses # 74, 77, and 80 in Tab. 3). All contours refer to the vertical alignment located at $r = s/2$ (vertical red lines in Fig. 12). In the benchmark coupled analyses, complete liquefaction is detected across most of the deep loose sand layer, for s/D = 4. This condition lasts until the end of the shaking in the upper part of the liquefiable layer, with a significant generation of excess pore water pressures also within the shallower dense sand. On the other hand, a closer drain layout (s/D = 2) prevents liquefaction triggering, together with a rapid dissipation of excess pore water pressures. Finally, intermediate results are obtained for the case s/D = 3, where liquefaction occurs at the boundary between the two layers, but the dissipation process starts before the end of the shaking.

As for the performance of the uncoupled approach, excess pore water pressures within the liquefiable layer tend to be slightly underestimated. The difference with respect to the coupled FE analyses, in terms of $r_{u\,max}$ computed at the centre of the loose sandy layer, amount to 36 %, 17 % and 10 %, for s/D = 2, 3 and 4, respectively. Nonetheless, considering the simplicity of the proposed method, the results are in a very good agreement with the coupled simulations and provide a reliable and insightful representation of the key physical mechanisms involved in the phenomenon, while strongly reducing computational time, as detailed below.

A further validation of the new uncoupled approach is proposed in Fig. 13 considering different shallow layers, a fixed spacing ratio (s/D = 3), and applying the scaled (SF = 0.280) 1995 Kobe (KO) earthquake as ground motion (analyses # 94 ÷ 96 in Tab. 3). Also for these configurations, the predictions from the uncoupled approach are in a good agreement with the results of the coupled FE analyses. Both the initial generation of excess pore water pressures and the subsequent dissipative phases are well captured by the proposed approach. The maximum differences between the two approaches amount to 3.7 % in terms of $r_{u\,max}$ for the configuration with a dense sand as shallow layer and to 34 % in terms of Δt_{ru} for the case of the homogeneous loose sand deposit. In the latter case (Figs. 13c and f), the uncoupled approach slightly overestimates the depth at which full liquefaction occurs: nevertheless, the

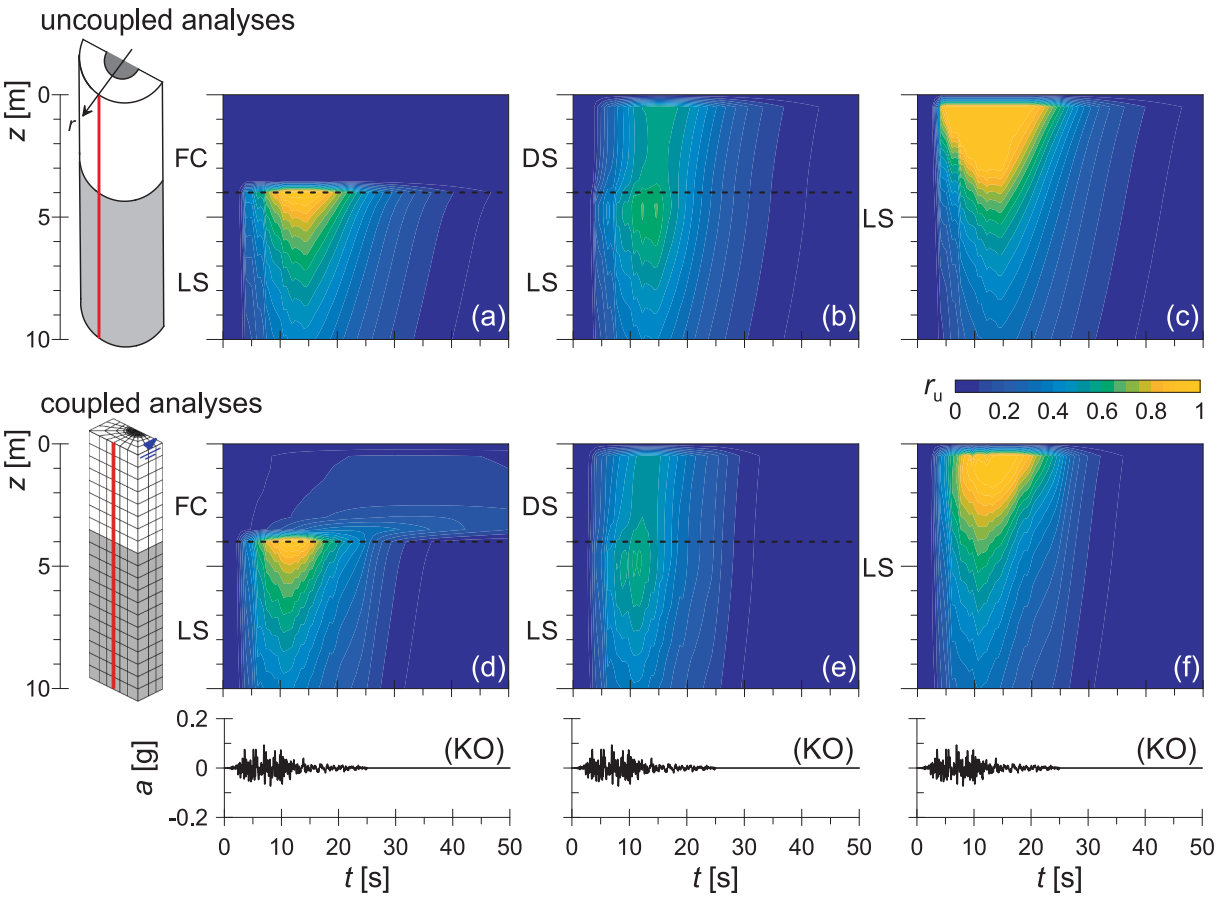

Fig. 13. Space-time contours of $r_u(z,t)$ considering a fine-grained crust (a, d); a shallow dense sand layer (b, e); or a homogeneous liquefiable sand (c, f), with $s/D = 3$ (seismic input = KO scaled by $SF = 0.28$).

overall agreement between the uncoupled and coupled analyses confirms that the proposed approach reliably reproduces the relevant features of the mechanical behaviour of layered soil deposits.

Finally, Fig. 14 shows the comparison between the values of $r_{u\ max}$ (a, b, and c), $\Delta t_{ru}/D_{5\text{-}95}$ (d, e, and f), and *LAI* (g, h, and i), resulting from the proposed uncoupled approach and the coupled FE analyses. The three parameters are computed along the same vertical alignment as that mentioned above, with $r_{u\ max}$ and $\Delta t_{ru}/D_{5\text{-}95}$ referring to the mid-depth within the liquefiable soil layer. Each chart provides the results for a given spacing ratio ($s/D = 2$, 3 and 4), for all earthquakes considered in this study and for all configurations (fine-grained, dense and loose shallow layer). For the sake of clarity, the analyses discussed in Figs. 12 and 13 are represented with blue and green symbols, respectively.

The uncoupled approach tends to underestimate $r_{u\ max}$ in the cases with a spacing ratio of $s/D = 2$. Nonetheless, as already discussed in Fig. 12, an underestimation of $r_{u\ max}$ of about 25 % at the centre of the liquefiable layer does not affect the overall accuracy of the uncoupled approach in representing the physical phenomenon. Considering all the analyses, the average differences in terms of $r_{u\ max}$ and $\Delta t_{ru}/D_{5\text{-}95}$ at the centre of the liquefiable layer are 15.1 % and 50 % for $s/D = 2$, 4.6 % and 25.6 % for $s/D = 3$, and 5.1 % and 17.3 % for $s/D = 4$, respectively. With reference to *LAI* (Figs. 14g, h, and i), the most notable discrepancies between the proposed uncoupled approach and the coupled FE analyses are detected in configurations characterised by very low values of the index, which are less relevant for the scope of this study. Indeed, when considering only configurations with $LAI \geq 0.4$ from the FE analyses, the average difference between the two approaches reduces to 15 %, compared to 25.1 % when all the analyses are taken into account.

Given the straightforward implementation of the proposed uncoupled approach and its capability of providing detailed spatial and temporal information on the liquefaction phenomenon in layered soil deposits equipped with gravel drains, which includes the generation, redistribution, and dissipation phases of excess pore water pressures, the differences discussed above may be considered acceptable. The proposed approach can therefore be deemed as a valuable tool for practical applications, especially in light of the significant computational saving compared to fully coupled analyses, which would imply a few minutes for the uncoupled approach versus several hours for a coupled 3D analysis, when run on a workstation equipped with a 24-core Intel Core i7–13700 CPU (2.1 GHz) and 32 GB of RAM.

5. Summary and conclusions

Although the effectiveness of gravel drains in mitigating the liquefaction hazard is well documented in the literature, their design still relies on simplified procedures that often neglect crucial features, such as the hydro-mechanical interaction between adjacent non-liquefiable layers in a stratified soil deposit. In the first part of this paper, an extensive series of fully coupled numerical analyses was presented, in which the liquefaction response of layered soil deposits was studied, both with and without vertical gravel drains. Exploiting the symmetry of the problem, a 3D unit cell was modelled in the FE programme *OpenSees* to represent an infinite system of drains. Different spacing ratios, soil types, and seismic inputs were considered to provide generality to the results.

The comparison between the numerical results of the 3D cell analyses and those referring to 1D free–field soil columns confirmed the efficiency of vertical gravel drains in mitigating liquefaction, by reducing both the maximum excess pore water pressures and duration over which these high values are maintained. The role of the hydraulic

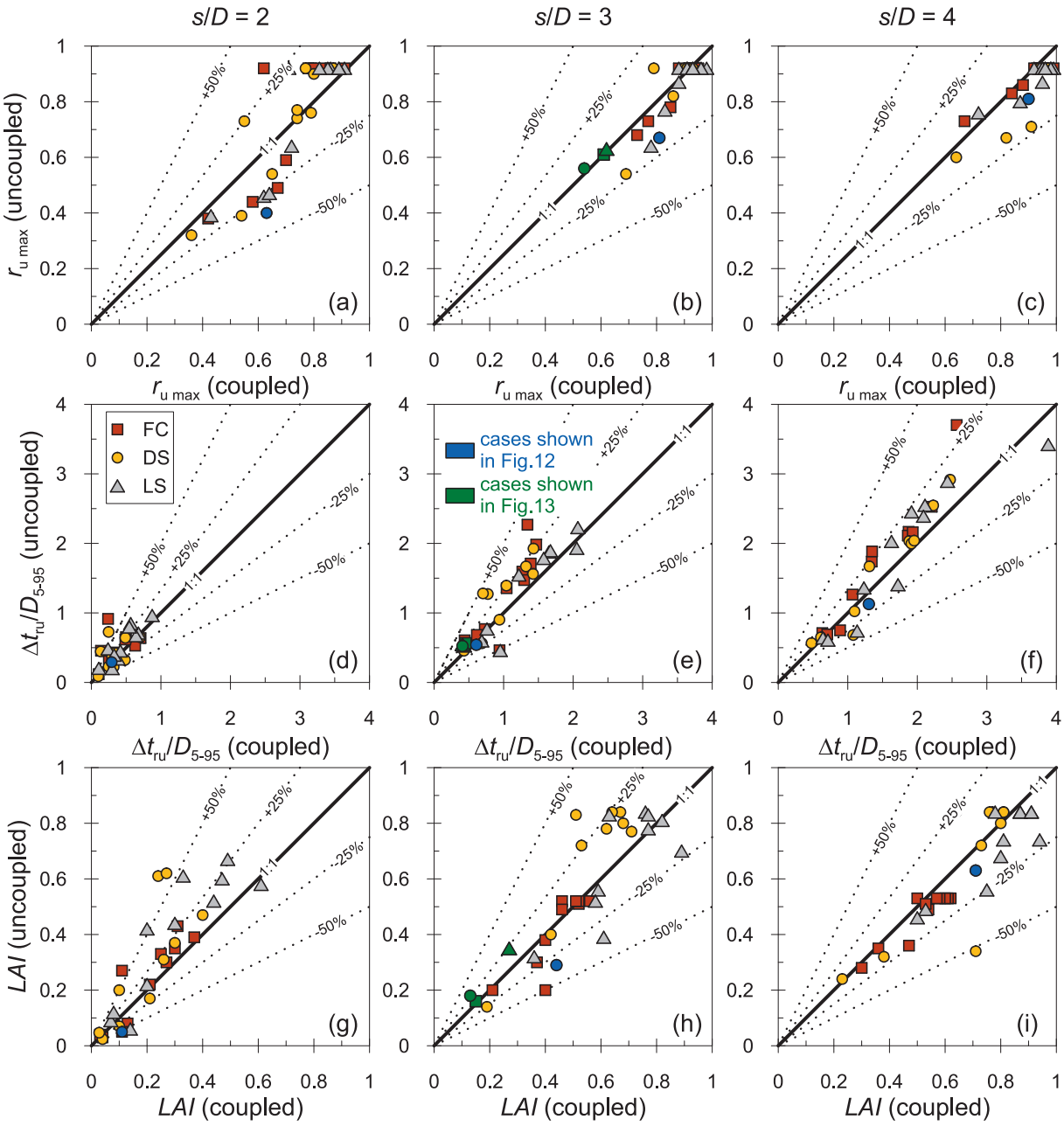

Fig. 14. Validation of the proposed uncoupled approach against the coupled results in terms of $r_{u\ max}$ (a, b, c), $\Delta t_{ru}/D_{5-95}$ (d, e, f), computed in the middle of the liquefiable layer, and *LAI* (g, h, i).

condition imposed by the shallow non–liquefiable layers turned out not to be negligible when describing the overall response of the system and the effectiveness of the gravel drains, especially near the interface between non–liquefiable and liquefiable layers.

An integral parameter was introduced to quantify both the efficiency of the gravel drains and the severity of liquefaction. This parameter accounts for the maximum excess pore pressure ratio and the dissipation time, thereby capturing the two primary benefits of vertical drains in improving the soil response. Depth–dependent weightings were not included in the current definition, although this aspect might be improved in design–oriented applications in the very next future.

The second part of the paper introduced an extension of the 1D uncoupled approach proposed by Boccieri et al. (2024) to an axisymmetric configuration with vertical gravel drains, to model the excess pore pressure generation and dissipation in stratified soil deposits subjected to seismic loading. Starting from the framework introduced by Onoue (1988), the proposed approach includes key improvements for the liquefaction risk assessment in the presence of vertical gravel drains, addressing known limitations of traditional uncoupled methods: (*i*) the assumption of uniform cyclic loading; and (*ii*) the inability to reproduce variations in frequency content due to pore pressure build–up. The novel uncoupled approach was implemented in a *Matlab* routine through the Finite Difference Method and compared with the fully coupled 3D FE analyses. The proposed method developed herein provides a reliable prediction of the overall liquefaction response, including the time evolution of pore pressure generation and dissipation, with a limited computational cost. It is also worth noting that the proposed approach can be easily extended to soil domains with more than just two layers.

Thanks to the quick response of the novel uncoupled approach, future developments will focus on the introduction of non-dimensional charts for the design of gravel drains, accounting for the influence of the hydraulic conductivity of the non-liquefiable layers on the

liquefiable soil and for the effects of the excess pore pressures redistribution within the soil domain.

CRediT authorship contribution statement

Gabriele Boccieri: Writing – original draft, Validation, Software, Methodology, Investigation, Data curation, Conceptualization. **Domenico Gaudio:** Writing – review & editing, Writing – original draft, Supervision, Software, Conceptualization. **Pedro Arduino:** Writing – review & editing, Supervision, Software, Conceptualization. **Riccardo Conti:** Writing – review & editing, Supervision, Methodology, Investigation, Funding acquisition, Conceptualization.

Declaration of competing interest

The authors declare that they have no known competing financial interests or personal relationships that could have appeared to influence the work reported in this paper.

Acknowledgments

This project was supported by Regione Lazio's programme POR-FSE 2014-2020, Italy, under grant agreement no. F85F21001280003.

Appendix A. – THE UNCOUPLED APPROACH BY BOCCIERI ET AL. (2024)

Starting from the seminal work by Seed et al. (1975), Boccieri et al. (2024) decompose the evaluation of seismic-induced excess pore water pressures within a 1D free-field soil column in two steps: (*i*) the assessment of earthquake-induced shear stresses, $\tau(z, t)$, through a 1D free-field total–stress site response analysis; (*ii*) the computation of excess pore water pressures via the solution of the modified 1D consolidation equation (Terzaghi, 1923), where a source term is added to consider pore–pressure generation due to seismic loading.

As for the evaluation of excess pore water pressures, the governing equation is (Seed et al., 1975):

$$\frac{\partial u(z,t)}{\partial t} = c_v \bullet \frac{\partial^2 u(z,t)}{\partial z^2} + \frac{\partial u_g(z,t)}{\partial t} \tag{A.1}$$

where c_v is the consolidation coefficient, which is computed as function of the current mean effective stress to account for the effect of pore pressure variations on soil stiffness. $\partial u_g(z,t)/\partial t$ is a source term representing the rate of excess pore water pressure build-up occurring in fully undrained conditions, which depends on soil liquefaction resistance and seismic-induced shear stresses. The source term requires the irregular time histories of shear stress, $\tau(t)$, to be reduced to an equivalent cyclic loading characterised by a constant amplitude $\tau_{eq} = 0.65 \bullet \tau_{max}$, an equivalent number of cycles N_{eq}, and a loading duration T_d. Accordingly, the source term can be rewritten as:

$$\frac{\partial u_g(z,t)}{\partial t} = \frac{\sigma'_{v0}}{N_L} \bullet \frac{dr_u}{dr_N} \bullet \frac{dN}{dt} \tag{A.2}$$

where σ'_{v0} is the geostatic vertical effective stress, N_L is the number of cycles to liquefaction, N is the n^{th} loading cycle, and $r_N = N/N_L$ is the cyclic ratio. Undrained cyclic laboratory tests are required to evaluate both the excess pore water pressure accumulation curve, r_u–r_N, from which the derivative dr_u/dr_N in Eq. (A.2) is obtained, and the liquefaction resistance curve, *CSR*-N_L, where $CSR = \tau/\sigma'_{v0}$ is the Cyclic Stress Ratio. The equivalent number of cycles, N_{eq}, was computed under the hypothesis of linear damage accumulation (Miner, 1945) and the peak-counting method (Hancock and Bommer, 2005), considering the curve *CSR*-N_L given by Eq. (8) as the locus of same damage level (*i.e.*, initial liquefaction). Accordingly:

$$N_{eq} = \frac{1}{2} \sum_{i=1}^{N_{hc}} X_i \tag{A.3}$$

with

$$X_i = \begin{cases} \left(\dfrac{|CSR_{0.65}| - CSR_t}{|CSR_i| - CSR_t} \right)^{-1/\eta} & if\ |CSR_i| > CSR_t \\ 0 & if\ |CSR_i| \le CSR_t \end{cases} \tag{A.4}$$

where N_{hc} is the total number of half cycles with amplitude τ_i in the time history $\tau(t)$, $CSR_{0.65} = \tau_{eq}/\sigma'_{v0}$ and $CSR_i = \tau_i/\sigma'_{v0}$. Eqs. (A.3) and (A.4) were also adopted to assess the cumulative distribution of the number of cycles, $N(t)$, with N_{hc} being the number of half cycles up to time t. This procedure overcomes the assumption of a uniform distribution of N_{eq} over the loading duration T_d, as initially proposed by Seed et al. (1975). Accordingly, the derivative dN/dt is not constant and must be computed numerically.

To account for the liquefaction-filtering of earthquake motion within liquefiable layers, an iterative procedure was developed based on the Stockwell transform (Stockwell et al., 1996) for the time–frequency decomposition of a signal. The key idea was to use the excess pore water pressures computed at the centre of the liquefiable layer at the k^{th} iteration, $r_{u,MID}(t)$, to identify when and how to filter the shear stresses $\tau(t)$ to be applied at the $(k+1)^{th}$ iteration. It was assumed that pore pressure ratios $r_{u,MID} < 0.2$ do not affect earthquake-induced shear stresses. For $r_{u,MID} > 0.2$, the high-frequency components of shear stresses are reduced by a factor $F\left(r^{max}_{u,MID}\right)$, where $r^{max}_{u,MID} = \max\left(r_{u,MID}\right)$:

$$F\left(r^{max}_{u,MID}\right) = 1 - a_1 \left(r^{max}_{u,MID} - 0.2\right)^{a_2} \tag{A.5}$$

where coefficients $a_1 = 0.65$ and $a_2 = 0.25$ were calibrated against the results of advanced fully coupled FE analyses, using a trial-and-error procedure. The filter F was applied to frequencies $f \ge 0.8 \cdot f_0$, where f_0 is the fundamental frequency of the soil deposit, as derived from total stress site response

analysis.

Being $S(t,f)$ the S-transform of the shear stress $\tau(t)$ at a given depth, the S-transform of the filtered shear stress, $\widehat{S}(t,f)$, was computed as:

$$\widehat{S}(t,f) = \widehat{F}(t,f) \bullet S(t,f) \tag{A.6}$$

where:

$$\widehat{F}(t,f) = \begin{cases} 1 & (t < \widehat{t}) \text{ or } (t \geq \widehat{t},\ f < 0.8f_0) \\ F\left(r_{\text{u,MID}}^{\max}\right) & (t \geq \widehat{t},\ f \geq 0.8f_0) \end{cases} \tag{A.7}$$

and $\widehat{t}$ is the first time instant when $r_{\text{u,MID}}$ reaches 0.2. The iterative procedure ends when:

$$\left| \frac{r_{\text{u,MID}}^{\max\ (k)} - r_{\text{u,MID}}^{\max\ (k-1)}}{r_{\text{u,MID}}^{\max\ (k-1)}} \right| \leq 1\% \tag{A.8}$$

Appendix B. – FD IMPLEMENTATION OF THE UNCOUPLED APPROACH

The governing equation of the new uncoupled approach (Eq. (5)) is approximated through the FD method and a FTCS scheme. As illustrated in Fig. B.1, the physical domain is represented through a *mesh* characterised by vertical and radial spatial discretisation, with step Δz and Δr respectively, and by a time discretisation, with step Δt. By adopting a uniform discretisation for both time and space domain, it follows:

$$\begin{aligned} t_{\text{n}} &= (n-1) \bullet \Delta t, \quad n = 1, \cdots, (N_{\text{t}}+1), \quad N_{\text{t}} = \frac{T_{\text{end}}}{\Delta t} \\ z_{\text{i}} &= (i-1) \bullet \Delta z, \quad i = 1, \cdots, (N_{\text{z}}+1), \quad N_{\text{z}} = \frac{H}{\Delta z} \\ r_{\text{j}} &= (j-1) \bullet \Delta r + R_D, \quad j = 1, \cdots, (N_{\text{r}}+1), \quad N_{\text{r}} = \frac{s/2 - R_D}{\Delta r} \end{aligned} \tag{B.1}$$

where T_{end} is the duration of the analysis and the axes-origin is fixed at the centre of the gravel drain.

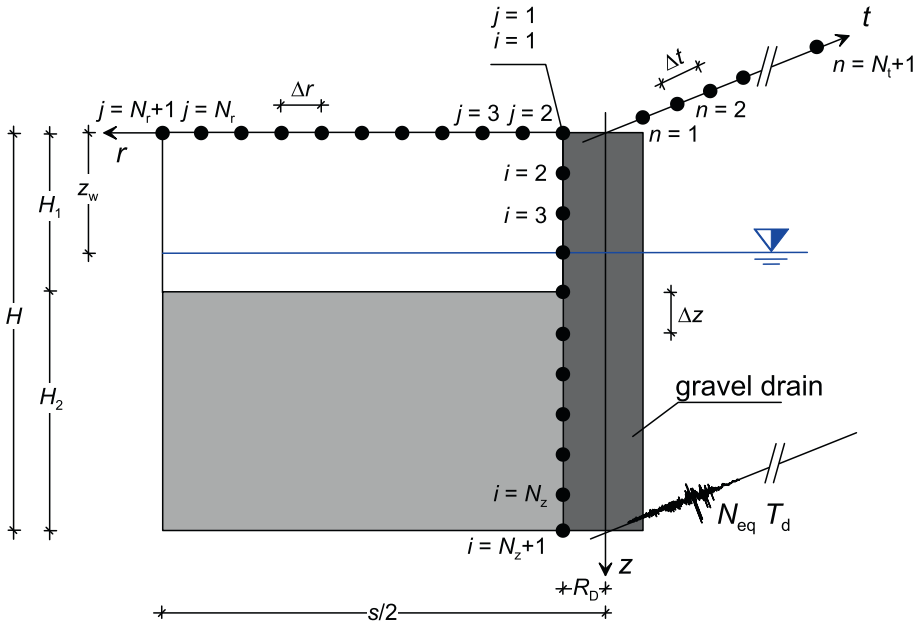

Fig. B.1. Numerical discretization of the physical domain.

Eq. (5) is solved within the soil domain in terms of the excess pore water pressure, $u_{\text{i,j}}^{\text{n+1}}$, at depth z_{i}, radial distance r_{j} and time $t_{\text{n+1}}$, to yield:

$$\begin{aligned} u_{\text{i,j}}^{\text{n+1}} &= u_{\text{i,j}}^{\text{n}} \bullet \left(1 - 2 \bullet B_{\text{i,j}}^{\text{n}} - 2 \bullet A_{\text{i,j}}^{\text{n}}\right) + u_{\text{i,j+1}}^{\text{n}} \bullet B_{\text{i,j}}^{\text{n}} \bullet \left(1 + \frac{\Delta r}{2 \bullet r_{\text{j}}}\right) + u_{\text{i,j-1}}^{\text{n}} \bullet B_{\text{i,j}}^{\text{n}} \bullet \left(1 - \frac{\Delta r}{2 \bullet r_{\text{j}}}\right) + \\ &+ A_{\text{i,j}}^{\text{n}} \bullet \left(u_{\text{i+1,j}}^{\text{n}} + u_{\text{i-1,j}}^{\text{n}}\right) + \Delta u_{\text{g,i,j}}^{\text{n+1}} \end{aligned} \tag{B.2}$$

where $A = c_{\text{vz}} \bullet \Delta t / \Delta z^2$ and $B = c_{\text{vr}} \bullet \Delta t / \Delta r^2$, in which c_{vr} and c_{vz} are the horizontal and vertical consolidation coefficients, respectively. Parameters A

and B are time–dependent, as the consolidation coefficients vary with the degradation of soil stiffness due to the pore pressures build–up, following the uncoupled approach by Boccieri et al. (2024). To guarantee the stability of the explicit FTCS scheme, it is necessary to impose the condition $A + B < 0.5$ at each point within the discretised domain.

Once the initial and boundary conditions, as suggested by Onoue (1988) and reported in §3, have been assumed, Eq. (B.2) can be solved. As for all nodes at the soil-drain interface ($r = R_D$), the flow continuity condition (Eq. (6)) must be satisfied. In the discretised form, the excess pore water pressure at each point along the soil–drain interface can be computed as follows:

$$-2 \bullet \frac{k_{hS} \bullet \Delta z^2}{k_{vD} \bullet R_D \bullet \Delta r} \bullet u_{i,2}^{n+1} = -2 \bullet \left(1 + \frac{k_{hS} \bullet \Delta z^2}{k_{vD} \bullet R_D \bullet \Delta r}\right) \bullet u_{i,1}^{n+1} + u_{i+1,1}^{n+1} + u_{i-1,1}^{n+1} \tag{B.3}$$

Eq. (B.3) results into a system of $(N_z - N_w)$ coupled equations, with $(N_z - N_w)$ unknowns, where $N_w = (z_w/\Delta z) + 1$ identifies the depth of the water table z_w. Finally, in the case of a stratified soil deposit, flow continuity (Eq. (7)) must be imposed at nodes $i_{H1} = (H_1/\Delta z) + 1$, which is discretised as follows:

$$u_{i_{H1},j}^{n+1} = \frac{k_{vS,i_{H1}+1} \bullet u_{i_{H1}+1,j}^{n+1} + k_{vS,i_{H1}-1} \bullet u_{i_{H1}-1,j}^{n+1}}{k_{vS,i_{H1}+1} + k_{vS,i_{H1}-1}} \tag{B.4}$$

where $k_{vSi_{H1}+1}$ and $k_{vS,i_{H1}-1}$ are the vertical hydraulic conductivities of the upper and lower soil layers, respectively.

Data availability

Data will be made available on request.

REFERENCES

Adamidis, O., Anastasopoulos, I., 2024. Cyclic liquefaction resistance of sand under a constant inflow rate. Géotechnique 74 (10), 1019–1032.

Adalier, K., Elgamal, A., 2004. Mitigation of liquefaction and associated ground deformations by stone columns. Eng. Geol. 72 (3–4), 275–291.

Asgari, A., Oliaei, M., Bagheri, M., 2013. Numerical simulation of improvement of a liquefiable soil layer using stone column and pile-pinning techniques. Soil Dyn. Earthq. Eng. 51, 77–96.

Azeiteiro, R.J., Coelho, P.A., Taborda, D.M., Grazina, J.C., 2017. Critical state–based interpretation of the monotonic behavior of Hostun sand. J. Geotech. Geoenv. Eng., ASCE 143 (5), 04017004.

Bessette, C., Dashti, S., Liel, A.B., Brito, L., 2025. Influence of Stratigraphic Variability and Ground Motion Properties on the Effectiveness of Dense Granular Columns as Liquefaction Mitigation for Structures. J. Geotech. Geoenv. Eng., ASCE 151 (5), 04025025.

Boccieri, G., Gaudio, D., Conti, R., 2024. An uncoupled approach for estimating seismic-induced pore water pressures in liquefiable sandy soils. Comput. Geotech. 170, 106266. https://doi.org/10.1016/j.compgeo.2024.106266.

Bol, E., Özocak, A., Sert, S., Çetin, K.Ö., Arslan, E., Kocaman, K., Ayhan, B.U., 2024. Evaluation of soil liquefaction in the city of Hatay triggered after the February 6, 2023 Kahramanmaraş-Türkiye earthquake sequence. Eng. Geol. 339, 107648.

Bouckovalas, G.D., Papadimitriou, A.G., Niarchos, D.G., Tsiapas, Y.Z., 2011. Sand fabric evolution effects on drain design for liquefaction mitigation. Soil Dyn. Earthq. Eng. 31 (10), 1426–1439.

Brennan, A.J., Madabhushi, S.P.G., 2002. Effectiveness of vertical drains in mitigation of liquefaction. Soil Dyn. Earthq. Eng. 22 (9–12), 1059–1065.

Conti, R., Angelini, M., Licata, V., 2020. Nonlinearity and strength in 1D site response analyses: a simple constitutive approach. Bull. Earthq. Eng. 18, 4629–4657. https://doi.org/10.1007/s10518-020-00873-5.

Croce, P., Flora, A., Modoni, G., 2014. Jet grouting: technology, design and control. Crc Press.

Cubrinovski, M., Rhodes, A., Ntritsos, N., Van Ballegooy, S., 2019. System response of liquefiable deposits. Soil Dyn. Earthq. Eng. 124, 212–229.

Cubrinovski, M., Ntritsos, N., 2023. 8th Ishihara lecture: Holistic evaluation of liquefaction response. Soil Dyn. Earthq. Eng. 168, 107777.

Dafalias, Y.F., Manzari, M.T., 2004. Simple plasticity sand model accounting for fabric change effects. Journal of Engineering Mechanics, ASCE 130 (6), 622–634.

De Gennaro, V., Canou, J., Dupla, J.C., Benahmed, N., 2004. Influence of loading path on the undrained behaviour of a medium loose sand. Can. Geotech. J. 41 (1), 166–180.

Elgamal, A., Lu, J., Forcellini, D., 2009. Mitigation of liquefaction-induced lateral deformation in a sloping stratum: Three-dimensional numerical simulation. J. Geotech. Geoenv. Eng., ASCE 135 (11), 1672–1682.

Flora, A., Bilotta, E., Valtucci, F., Fierro, T., Perez, R., Santucci de Magistris, F., Aysal, N., 2024. Liquefaction effects in the city of Gölbaşı: from the analysis of predisposing factors to damage survey. Eng. Geol. 107633.

García-Torres, S., Madabhushi, G.S.P., 2019. Performance of vertical drains in liquefaction mitigation under structures. Bull. Earthq. Eng. 17, 5849–5866.

Gaudio, D., Seong, J., Haigh, S., Viggiani, G.M.B., Madabhushi, S.P.G., Shrivatsava, R., Veluvolu, R., Padhy, P., 2023. Boundary effects on dynamic centrifuge testing of onshore wind turbines on liquefiable soils. Int. J. Phys. Mod. Geotech. 23 (1), 16–34. https://doi.org/10.1680/jphmg.21.00085.

Gu, Q., Conte, J.P., Yang, Z., Elgamal, A., 2011. Consistent tangent moduli for multi-yield-surface J2 plasticity model. Comput. Mech. 48, 97–120.

Hancock, J., Bommer, J.J., 2005. The effective number of cycles of earthquake ground motion. Earthq. Eng. Struct. Dyn. 34 (6), 637–664.

Howell, R., Rathje, E.M., Kamai, R., Boulanger, R., 2012. Centrifuge modeling of prefabricated vertical drains for liquefaction remediation. J. Geotech. Geoenv, Eng., ASCE 138 (3), 262–271.

Kuhlemeyer, R.L., Lysmer, J., 1973. Finite element method accuracy for wave propagation problems. Journal of the Soil Mechanics and Foundations Division 99 (5), 421–427.

Martin, J.R., Olgun, C.G., Mitchell, J.K., Durgunoglu, H.T., 2004. High-modulus columns for liquefaction mitigation. J. Geotech. Geoenv, Eng., ASCE 130 (6), 561–571.

Mathworks Inc., 2021. Matlab version 9.10.0 (R2021a). Natick, Massachusetts.

McGann, C.R., Arduino, P., Mackenzie-Helnwein, P., 2015. A stabilized single-point finite element formulation for three–dimensional dynamic analysis of saturated soils. Comput. Geotech. 66, 126–141.

McKenna, F., Fenves, G.L., Scott, M.H., Jeremić, B., 2000. Open System for Earthquake Engineering simulation. University of California Berkeley, Berkeley, CA, USA.

Mele, L., Tian, J.T., Lirer, S., Flora, A., Koseki, J., 2019. Liquefaction resistance of unsaturated sands: experimental evidence and theoretical interpretation. Géotechnique 69 (6), 541–553.

Minaka, U.S., Okamura, M., Ono, K., 2021. Verification of effectiveness and design procedure of gravel drains for liquefaction remediation. Soils Found. 61 (5), 1191–1206.

Miner, M.A., 1945. Cumulative damage in fatigue. Trans. ASME 67, A159–A164.

Moug, D.M., Bray, J.D., Bassal, P., Macedo, J., Ulmer, K., Cetin, K.Ö., Bikçe, M., 2024. Liquefaction-induced ground and building interactions in İskenderun from the 2023 Kahramanmaraş earthquake sequence. Earthq. Spectra 40 (2), 913–938.

Nishio, N., Tamaoki, K., Machida, Y., 1985. Dynamic deformation characteristics of crushed gravel by means of large-size triaxial test apparatus. *In Proceedings of the 20th annual convention, Japanese society of soil mechanics and foundation engineering*, (p. 603-4). Tokyo, Japan.

Ntritsos, N., Cubrinovski, M., 2024. Ground-motion effects on liquefaction response. Soil Dyn. Earthq. Eng. 177, 108392.

Onoue, A., 1988. Diagrams considering well resistance for designing spacing ratio of gravel drains. Soils Found. 28 (3), 160–168.

Potts, D., Zdravković, L., 1999. Finite element analysis in geotechnical engineering: Theory. Thomas Telford, London.

Rathje, E.M., Abrahamson, N.A., Bray, J.D., 1998. Simplified frequency content estimates of earthquake ground motions. J. Geotech. Geoenv. Eng., ASCE 124 (2), 150–159.

Recktenwald, G.W., 2004. Finite-difference approximations to the heat equation. Mech. Eng. 10 (01).

Seed, H.B., Booker, J.R., 1977. Stabilization of potentially liquefiable sand deposits using gravel drains. J. Geotech. Eng. Div. 103 (7), 757–768.

Seed, H.B., Idriss, I.M., 1970. *Soil moduli and damping factors for dynamic response*. Berkeley, California: Report No. EERC 70-10, Earthquake Engineering Research Centre.

Seed, H.B., Martin, P.P., Lysmer, J., 1975.The generation and dissipation of pore water pressures during soil liquefaction. College of Engineering, University of California.

Sinatra, L., Foti, S., 2015. The role of aftershocks in the liquefaction phenomena caused by the Emilia 2012 seismic sequence. Soil Dyn. Earthq. Eng. 75, 234–245.

Stockwell, R.G., Mansinha, L., Lowe, R.P., 1996. Localization of the complex spectrum: the S transform. IEEE Trans. Signal Process. 44 (4), 998–1001.

Tang, L., Zhang, X., Ling, X., 2016. Numerical simulation of centrifuge experiments on liquefaction mitigation of silty soils using stone columns. KSCE J. Civ. Eng. 20, 631–638.

Die Berechnung der Durchassigkeitsziffer des Tones aus dem Verlauf der hydrodynamischen Spannungs 2A 132, 1923, 105–124.

Trifunac, M.D., Brady, A.G., 1975. A study on the duration of strong earthquake ground motion. Bull. Seism. Soc. Am. 65 (3), 581–626.

Vucetic, M., Dobry, R., 1991. Effect of soil plasticity on cyclic response. J. Geotech. Eng. 117 (1), 89–107.

Yang, Z., Elgamal, A., Parra, E., 2003. Computational model for cyclic mobility and associated shear deformation. J. Geotech. Geoenv. Eng., ASCE 129 (12), 1119–1127.
Yang, Z., Lu, J., Elgamal, A., 2008. OpenSees soil models and solid-fluid fully coupled elements. User's Manual. Ver, 1, 27.
Zienkiewicz, O.C., Chang, C.T., Bettess, P., 1980. Drained, undrained, consolidating and dynamic behaviour assumptions in soils. Géotechnique 30 (4), 385–395.